Biomaterials Science



PAPER



Cite this: *Biomater. Sci.*, 2020, **8**, 5071

Received 15th May 2020, Accepted 28th July 2020 DOI: 10.1039/d0bm00805b

rsc.li/biomaterials-science

In vitro and in vivo studies on ultrafine-grained biodegradable pure Mg, Mg—Ca alloy and Mg—Sr alloy processed by high-pressure torsion

Wenting Li,^a Xiao Liu,^a Yufeng Zheng, ¹ Wenhao Wang,^b Wei Qiao,^b Kelvin W. K. Yeung,^{*b} Kenneth M. C. Cheung,^b Shaokang Guan,*^c Olga B. Kulyasova^d and R. Z. Valiev*^d

High-pressure torsion (HPT) can refine the microstructure and consequently modify the properties, such as mechanical and corrosion properties, of Mg and its alloys. Biodegradable magnesium materials alloyed with the essential elements of life, such as Ca and Sr, are a current research frontier. In this study, biodegradable ultrafine-grained pure Mg, Mg–Ca alloy, and Mg–Sr alloy were prepared using HPT processing. The microstructure, mechanical properties, biodegradable behaviors, and biocompatibility *in vitro* and *in vivo* of these materials were systematically investigated. Our results revealed that HPT pure Mg with a bimodal and ultrafine-grained microstructure showed higher mechanical strength, ductility, and degradation rate compared with the as-received materials. The good biocompatibility of HPT pure Mg was confirmed both *in vitro* and *in vivo*. The HPT Mg–Ca alloy and Mg–Sr alloy with homogeneous ultrafine-grained microstructures showed higher mechanical strength and lower degradation rate than their as-cast counterparts. The good biocompatibility of the HPT Mg–Ca alloy and Mg–Sr alloy was also revealed. All these findings indicate that HPT is an alternative avenue to fabricate biodegradable Mg-based materials.

Introduction

Biodegradable magnesium alloys have been recently developed as desirable materials for orthopedic implants.¹⁻³ Biodegradable Mg and its alloys can degrade gradually in the physiological environment, evading second surgery for implant removal and alleviating the physical and financial burden for patients. Also, the elastic modulus of biodegradable magnesium is close to natural bone, avoiding the 'stress shielding' effects of traditional metallic implants and the corresponding bone loss.⁴ Besides, Mg is an essential element that plays a critical role in bone tissue.^{5,6} It was revealed that Mg implants were able to promote osteogenic differentiation and improve bone-fracture healing.⁷

There has been a large number of investigations focused on optimizing the comprehensive properties, including the mechanical and degradation properties of biodegradable mag-

nesium materials. One of the approaches is alloying Mg with different elements. However, the traditional industrial magnesium alloys alloyed with Al, Mn, Zn, RE, Zr, Ag, and Y should be carefully considered when used in the orthopedic field. There is a possibility of excessive release of these alloying elements, which are permitted at a very low limit in our body.^{1,8} Choosing the essential elements of life that can help bone healing as alloying elements is a desirable way to develop new biodegradable Mg alloys.4 Based on this developing strategy, our research team previously developed Mg-Ca alloy and Mg-Sr alloy for orthopedic applications. 9,10 Ca, as the main constituent of bone apatite, is involved in bone metabolism, activating Ca-sensing receptors of osteoblast cells and promoting osteoblast proliferation, differentiation and extracellular matrix mineralization. 11,12 Sr is of importance in the formation of bone matrix mineralization and is utilized as a promising agent to treat osteoporosis. 13,14 The implantation of Mg-Ca alloy in rabbit femoral shafts improved the activity of the surrounding osteoblasts and osteocytes. Significantly increased cortical bone thickness and bone mineral density, as well as newly formed endosteal bone were observed around the Mg-2Sr alloy implanted in mice femur compared with the control.10

Although Mg-Ca alloy and Mg-Sr alloy were promising as orthopedic materials, one of the challenges is how to improve

^aDepartment of Materials Science and Engineering, College of Engineering, Peking University, Beijing 100871, China. E-mail: yfzheng@pku.edu.cn ^bDepartment of Orthopedics and Traumatology, The University of Hong Kong, Pokfulam, Hong Kong, China

^cSchool of Materials Science and Engineering, Zhengzhou University, Zhengzhou 450001, China

 $[^]d$ Ufa State Aviation Technical University, 12 Karl Marx Street, Ufa 450008, Russia

their mechanical properties and degradation behaviors simultaneously. HPT is a process during which high pressure and concurrent high shear strain are imposed on a disk.¹⁵ It can extremely refine the microstructure and consequently modify the properties, such as mechanical and corrosion properties, of Mg and its alloys. 16 Although traditional plastic deformation, such as rolling and extrusion, also can modify the microstructure of Mg and its alloys, resulting in the improvement of the properties, 2,17 the limited number of dislocation slip systems of magnesium materials resulting from their hexagonal close-packed (HCP) structure impedes the improvement, 18 and high temperature is needed during the processing, which restricts the effectiveness of strain hardening mechanisms. Severe plastic deformation processing during which high plastic strains and hydrostatic pressure were imposed on the specimens can help to overcome this limitation and to obtain bulk nanostructured materials with excellent properties. 19,20 HPT and equal channel angular pressing (ECAP) are two kinds of attractive severe plastic deformations. According to previous studies, using HPT to obtain ultrafinegrained or nanograined microstructure of Mg alloys is more feasible than using ECAP, 21 for the reason that the higher temperature during ECAP causes less effective grain refinement. HPT was reported to effectively decrease the grain size of the as-cast pure Mg to a few micrometers or several hundred nanometers and improve the strength. 22,23 The influence of HPT processing on corrosion resistance of pure Mg is controversial. Some investigators found that HPT enhanced corrosion resistance of pure Mg,24,25 while others believed that HPT had no evident influence on the corrosion resistance of pure Mg.²² Cláudio L. P. Silva et al. 26 observed that HPT pure Mg exhibited similar corrosion potential but higher polarization resistance in comparison with the as-received pure Mg. Besides, the biocompatibility of HPT pure Mg was acceptable according to cytotoxicity tests using human osteosarcoma cell line.24,26 Magnesium alloys, such as AZ31, 24,25 AZ91, 24,25 WE43, 27,28 Mg–Zn alloy, ²⁹ Mg–Zn–Ca alloy, ^{30,31} Mg–Li alloy³² and Mg–rare earth alloys³³⁻³⁶ were processed by HPT and obtained significant grain refinement as well as excellent mechanical properties. There is also no explicit agreement on the change of corrosion tendency of these alloys caused by HPT. HPT Mg-Zn-Ca alloy showed lower corrosion rate in comparison with its extruded counterpart, and uniform corrosion of this HPT material was revealed.³⁷ Debora R. Lopes et al.²⁴ reported that HPT could decrease the degradation rate of AZ31 and AZ91 alloys in Hank's solution while increasing that of ZK60 alloy. E. A. Lukyanova et al.²⁸ observed that the corrosion resistance of WE43 after HPT was increased. Besides, the cytotoxicity of magnesium and its alloys processed by HPT was only evaluated in a few studies.24,26 Such a broad diversity of the results regarding the effects of HPT on properties of magnesium materials indicated the need for researchers to comprehensively investigate the properties of HPT pure Mg and Mg-Ca and Mg-Sr alloys.

This is the first study that evaluates the *in vivo* degradation behavior and biological performance of HPT Mg and its alloys,

to the best of our knowledge. The influence of HPT on the overall performance of pure Mg, Mg–Ca alloy, and Mg–Sr alloy was investigated for the first time. The goal of this research is to reveal the effect of HPT on the microstructure, mechanical properties, biodegradation behavior, cytocompatibility, and bone formation ability of pure Mg, Mg–Ca alloy and Mg–Sr alloy.

Experimental materials and procedures

HPT specimen preparation

The as-cast commercial pure Mg (99.98%) disk, as-cast Mg-1Ca alloy (which was detailed in our previous paper⁹) disk and as-cast Mg-2Sr alloy (which was described in our earlier article¹⁰) disk with a diameter of 20 mm and thickness of 1.0 mm were processed by HPT. The as-cast Mg-1Ca alloy was prepared from pure Mg (99.98%) and Ca (99.9%) metal powders in a graphite crucible under the protection of SF₆ and CO2. The as-cast Mg-2Sr alloy was prepared using pure Mg (99.98%) and Mg-10Sr master alloy in the graphite crucible under the protection of SF₆ and CO₂. Nominal and actual compositions of the materials are listed in Table 1. To avoid incipient melting and to equalize the chemical composition, the samples were homogenized before HPT at a temperature of 450 °C for 24 hours, followed by cooling in water. Then they were put between two anvils under a compressive pressure (P) of 6 GPa at room temperature to 5 turns (N) with a rotation speed of 1 rpm. Besides, the three as-cast materials before and after hot extrusion (The extruded materials were obtained at 210 °C with an extrusion rate of 2 mm s⁻¹ and extrusion ratio of 1/17.) were also used in this study for comparison.

Nanoindentation test

The nanoindentation test was conducted with Tribo Indenter (Hysitron, USA) on the polished surfaces of the three HPT materials. The experiments were performed along two perpendicular diameters (shown in Fig. 1(b)) on the disk's surface (ground up to 7000 grit). The Berkovich diamond pyramid tip was used in load-controlled mode with a loading rate of 40 μN s $^{-1}$ to a maximum loading of 400 μN . The indenter was held at the maximum load for 2 s before unloading at the rate of 40 μN s $^{-1}$. The Oliver–Pharr method 38 was utilized for determining elastic modulus and hardness.

Table 1 Compositions of the experimental materials

	Composition (wt%)						
Material	Ca/Sr	Fe	Ni	Cu	Mg		
Pure Mg Mg–1Ca Mg–2Sr	— Ca1.06 Sr0.98	0.0057 0.0052 0.0049	0.00072 0.00061 0.00059	0.00083 0.00079 0.00062	99.98 Bal. Bal.		

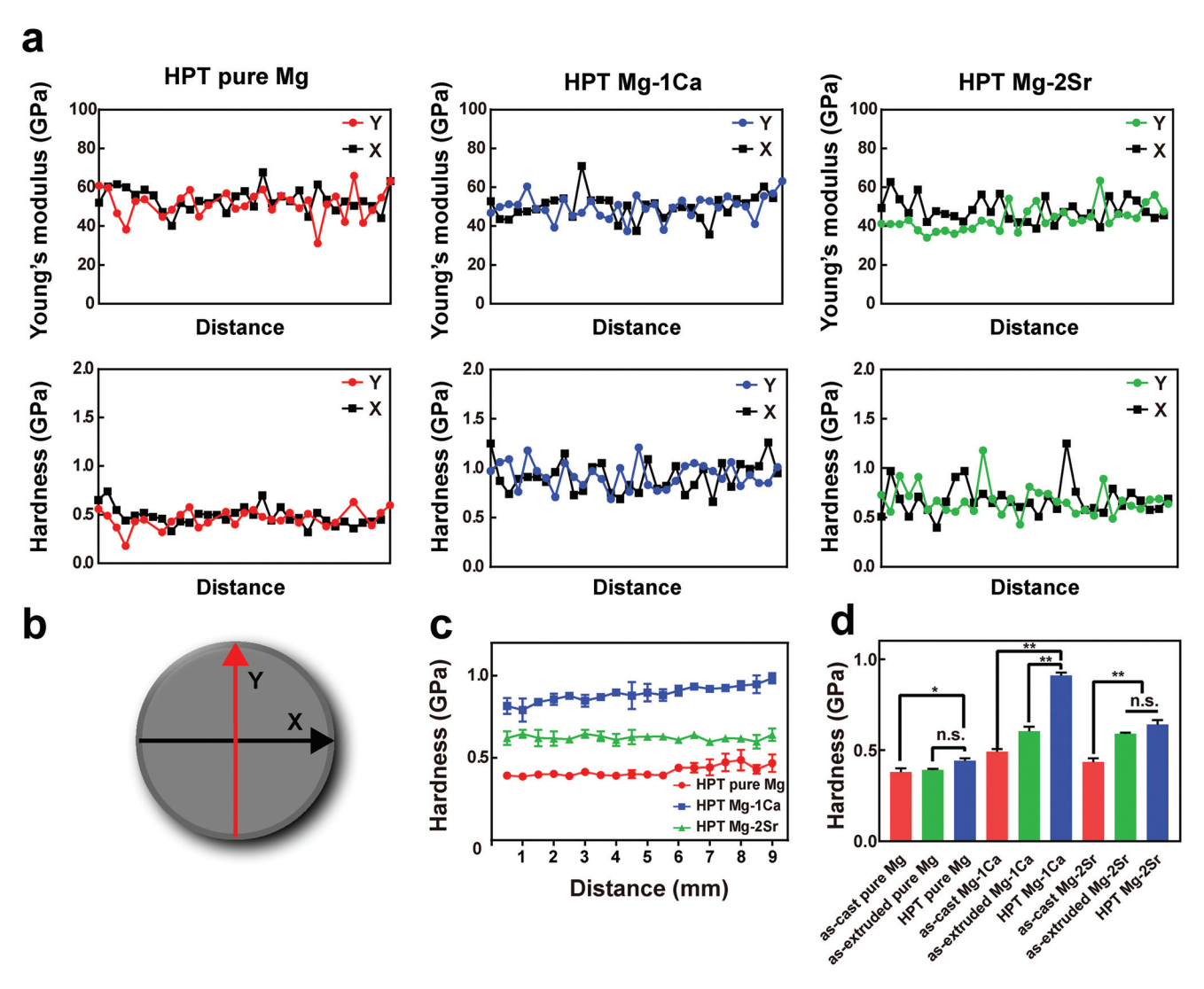


Fig. 1 The homogeneity evaluation of pure Mg, Mg-1Ca alloy, and Mg-2Sr alloy after HPT processing. (a) The Young's modulus and hardness obtained by nanoindentation tests along two diameters perpendicular to each other (b) of the three HPT materials. The x-axis from left to right represents the position along the diameter from left to right (X) or from bottom to top (Y). (c) The change of Vickers hardness of the three HPT materials with the increase of the distance from the central point of the disk. (d) The average Vickers hardness of the three HPT materials after different processing procedures.

Microhardness evaluation

The Vickers hardness across two perpendicular diameters of the three HPT materials was evaluated with a micro-hardness tester (SHIMADZUHMV-2t) using a Vickers indenter. The distance of 0.5 mm between two indentations was kept during the tests. The indentation load was 980.7 mN and maintained for 10 s. The average hardness of the as-cast and as-extruded samples was also tested.

Microstructure evaluation

The specimens were ground to 5000 grit and then electrochemically polished in a solution containing phosphoric acid (250 mL), glycerol (10 mL), alcohol (750 mL), and citric acid (0.5 g). Microstructure analysis was performed using an optical microscope (Olympus BX51M) and environmental scanning

electron microscope (ESEM, FEI Quanta 200F, Holland). Cu K α radiation was utilized to characterize the phase composition and texture of the samples through X-ray diffraction (XRD, Rigaku DMAX 2400, Japan) at a step size of 0.02° from 10° to 90° . The materials processed by HPT were also characterized by transmission electron microscopy (TEM, Tecnai G2 F20, USA) at 200 kV. TEM samples were obtained using ion milling (Gatan Model 691PIPS, USA). The grain size of the samples before and after extrusion was analyzed according to the mean linear intercept method, and the average value of individual grains of HPT samples was calculated.

Micro-tensile test

The micro-tensile specimens (gauge length 4 mm, width 2 mm, thickness 1 mm (Fig. 4(a)) were cut from the disks.

Micro-tensile tests were performed at an initial strain rate of $1.0 \times 10^{-3}~{\rm s}^{-1}$ on a mechanical test machine (Instron Micro Tester 5843) at room temperature. The yield strength (YS) was calculated according to the stress at which 0.2% plastic deformation occurs. At least three tests were conducted for each material. Then the fracture morphology was observed by ESEM.

In vitro degradation behavior test

In vitro degradation behaviors were investigated by immersing the samples in Hank's solution. The specimens were cut into small disks with a diameter of 8 mm and a height of 1 mm, and they were ground up to 2000 grit. The ratio of surface area to solution volume ratio was kept 20 ml cm⁻² during the tests according to ASTM-G31-72. The pH value of the solution and the hydrogen release volume was recorded after 4, 8, 12, 24, 72, 120, 168, and 336 h. The corrosion products were removed using a solution composed of CrO₃ (200 g L⁻¹) and AgNO₃ (2 g L⁻¹) after 12, 24, 168, and 336 h. Then the samples were weighed after being rinsed with DI water and dried. The weight loss ratio was determined using the following equation:

 $\frac{\text{initial weight} - \text{weight at the respective time point}}{\text{initial weight}} \times 100\%$

ESEM was utilized to observe the material surface.

Cytotoxicity

The indirect cell culture method was used to assess the cytotoxicity of these three HPT materials in comparison with their as-extruded counterparts. MC3T3-E1 cells and human mesenchymal stem cells (hMSCs) were seeded at a density of 3 \times 10 3 cells per well on a 96-well tissue culture plate. They were cultured in Dulbecco's modified Eagle's medium (DMEM) with 10% fetal bovine serum (FBS) and 1% penicillin/streptomycin (PS). After overnight incubation for cell attachment, the culture medium was replaced with extracts which were prepared by immersing samples into culture medium with a surface area to solution volume ratio of 1.25 mL cm⁻² under standard cell culture conditions for 24 h. After 1, 3, and 5 days of incubation, the medium was removed and rinsed slightly with phosphate-buffered saline (PBS) three times. DMEM containing 10% Cell Counting Kit-8 (CCK8, Dojindo Molecular Technologies, Japan) was then added into the well. After 1 h, the spectrophotometric absorbance (OD) was recorded at 450 nm using a multimode detector (Bio-Rad 680, USA). The cells cultured in normal culture medium with 10% FBS and 1% PS for 1, 3, and 5 days were used as the negative control. The cell viability value was determined by dividing the OD value of the experimental group by the value of negative control.

Surgical procedure

The animal experiments were authorized by the Licensing Office of the Department of Health of the Hong Kong Government and University Ethics Committee of the University of Hong Kong. All animal procedures were performed in accordance with the Guidelines for Care and Use of Laboratory Animals of Laboratory Animal Unit of the University of Hong Kong and approved by the Animal Ethics Committee of the University of Hong Kong. Investigations were carried out on 3-month old female Sprague-Dawley (SD) rats that were provided by the Laboratory Animal Unit of the University of Hong Kong. Before the operation, xylazine (6 mg kg⁻¹) and ketamine (67 mg kg⁻¹) were injected into the rats' enterocoelia to anesthetize the rats. Cylindrical rods (diameter 1.0 mm, height 6.0 mm) were machined from these three HPT materials' disks, and were polished and sterilized before implantation surgery. The axial direction of the cylinder is parallel to the surface of the disc. In total, 18 rats were randomly assigned to three groups of 6 animals each. A tunnel defect with a diameter of 1 mm was created at the femur lateral epicondyle followed by the insertion of these three HPT implants. Muscle and skin incisions were sutured layer-by-layer. To minimize the suffering of rats, oxytetracycline (60 mg kg⁻¹) was injected into rats in a 72-hour interval for the initial 6 days postoperation. Besides, flunixin (2.5 mg kg⁻¹) was also given as an analgesic in 12 h intervals for the initial 3 days postoperation.

Micro-computed tomography and histological analysis

The gradual change of implant and bone in the vicinity of the implant was monitored using a micro-computed tomography (micro-CT) scanning device (SkyScan 1076, Belgium) when the animals were under anesthesia at the indicated time points. The voxel size is 17.33 μ m. All the rats were monitored by micro-CT. The raw data were reconstructed by NRecon (Skyscan Company). CTVol was utilized to generate 3D models of bone and implant, and CTAn was used to analyze the change of implant and the surrounding bone. The *in vivo* degradation rate was determined using micro-CT results based on the following equation: ³⁹

$$C = (V_t - V_0)/At,$$

where C is the degradation rate, V_t is the implant volume at defined time points during the implantation period, V_0 is the implant volume when the operation was just completed, A is the original surface area of the implant, and t is time after surgery.

Rats were euthanized at 24 weeks postoperation, and then the femurs were isolated. The femurs were fixed in 10% buffered formalin, and then some of them were processed in gradient ethanol for the preparation of non-decalcified sections after 48 h. After immersion in xylene for 3 days, femurs were transferred to methyl-methacrylate (MMA). Finally, the femurs after embedding were machined into thin slices and then were polished from a thickness of ~250 μm to ~40–60 μm . Giemsa staining was conducted on these slices. For decalcified sections, after fixation with 10% buffered formalin, the femurs were decalcification in 10% ethylenediaminetetraacetic acid for 4–6 weeks. The implants were carefully

pulled out from the harvested femur. The femurs were then dehydrated in 70%, 95%, and 100% ethanol, and finally, paraffin was used to embed the femurs. The slices with a thickness of 5 μ m were obtained using a microtome (RM215, Leica Microsystems, Germany). Hematoxylin staining was conducted in the represented slices. Sections were then observed using microscopy (Nikon, Tokyo, Japan).

Statistical analysis

All data were expressed as means \pm standard deviation. The difference between groups was analyzed using one-way analysis of variance (ANOVA) followed by the Tukey test. The level of significant difference among groups was defined and noted as *p < 0.05, **p < 0.01.

Results

Hardness and modulus along the diameter of the disk

Different strains were imposed on the samples from the center to the edge during HPT processing, so the microstructure might be inhomogeneous.¹⁵ It is reported that there is also a potential for materials to achieve homogeneous microstructures and properties when the appropriate parameters were used during this processing, such as a high enough number of revolutions.^{40,41} The grains either at the center area or the edge area of the disk could be refined completely, and the microstructures could become homogeneous once the shear strain reached a particular value.⁴² The measure-

ments of local hardness across the diameter from one edge of the disk to another edge along the diameter had been widely used to detect whether the material is homogeneous or not. 15,43 The results of nanoindentation tests along two diameters perpendicular to each other (Fig. 1(b)) are shown in Fig. 1(a), and the data indicated no significant distinction of elastic modulus or hardness values in the center of the disk and peripheral regions for all these three materials. The shape of indentation after nanoindentation tests is 3-sided pyramid, and the projected area (residual indentation area) is 10-20 µm² for nanoindentation tests. The data of Vickers hardness with increasing distance from the center of the disk are shown in Fig. 1(c), indicating the uniformity with no significant difference of the hardness with the increment of the distance from the central point for each material. The shape of indentation after microhardness tests is 4-sided pyramid, and the impression diagonal of its projected image is 40-70 μm. These results indicated that the three HPT materials might have uniform microstructures and properties.

Microstructure

Fig. 2(a) and 3 show the representative microstructures of these three materials after different processing. Both hot extrusion and HPT processing refined the microstructure of the as-cast pure Mg. The grain size of the as-cast pure Mg was 1.0 ± 0.8 mm and decreased to 88 ± 18 µm after hot extrusion. A bimodal microstructure of HPT pure Mg is shown in the TEM bright-field images (Fig. 3(a), (d) and (e)) and was com-

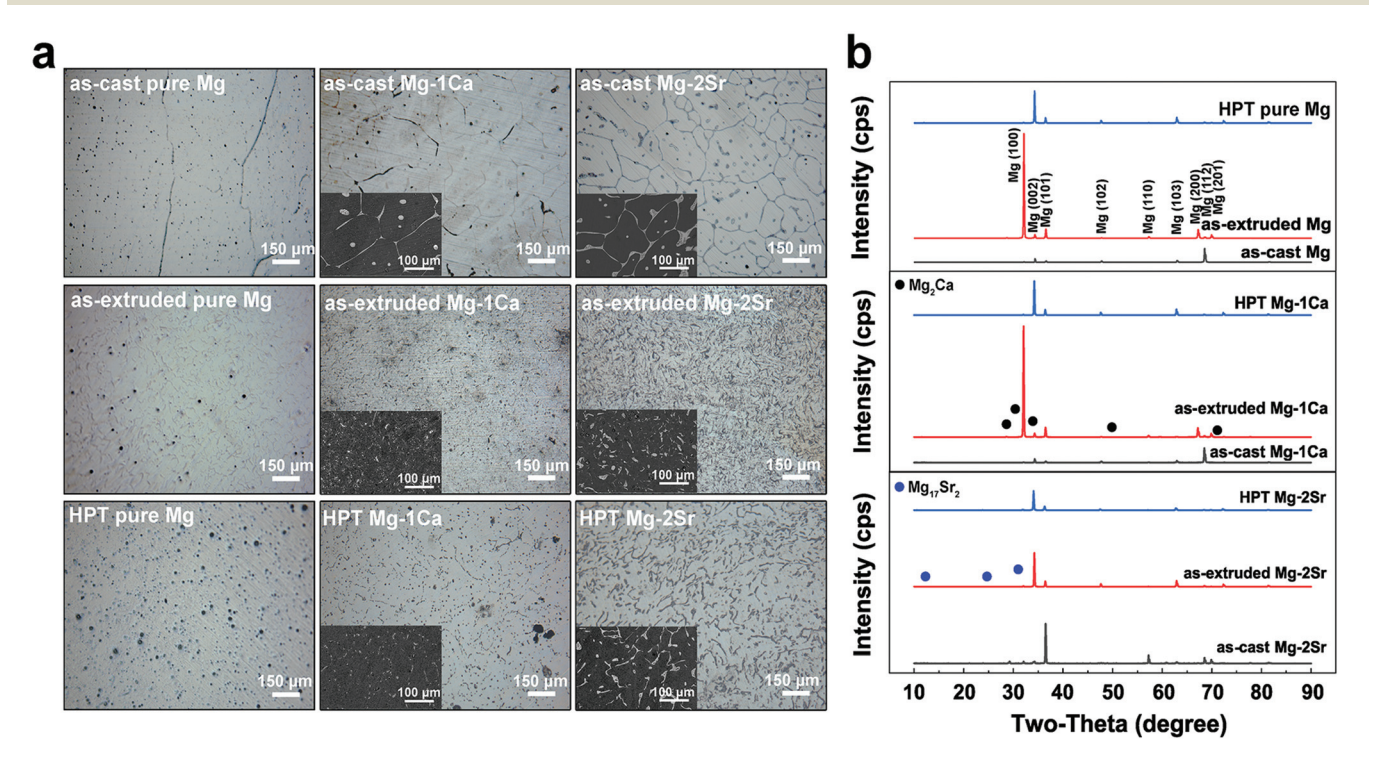


Fig. 2 Microstructures and phase composition of pure Mg, Mg-1Ca and Mg-2Sr alloys. (a) Microstructures observed using an optical microscope and ESEM images at the lower left. (b) XRD patterns of these materials.

posed of larger grains with the size of 1.8 \pm 0.5 μm and finer grains with the size of 590 \pm 120 nm. The selected area electron diffraction (SAED) pattern (Fig. 3(a)) presented diffraction rings indicating high misorientation between the grains. 15 The microstructures of Mg-Ca alloy and Mg-Sr alloy were also significantly refined by HPT. The grain size of the as-cast Mg-Ca was 183 \pm 10 μ m (Fig. 2(a)). The grain was refined by extrusion and HPT to the size of 57 \pm 7 μm (Fig. 2(a)) and 171 \pm 52 nm (Fig. 3(b)), respectively. HPT Mg-Ca alloy in the TEM bright-field image exhibited homogeneous distribution of ultrafine grains. The SAED pattern of HPT Mg-Ca alloy showed clustered diffraction spots and rings (Fig. 3(b)). The as-cast Mg-Sr alloy had coarse grains with the size of 170 \pm 20 μm and the as-extruded Mg-Sr alloy had finer grains of 53 \pm 10 μ m. HPT Mg-Sr alloy presented an ultrafine-grained structure with a grain size of 720 \pm 180 nm (Fig. 3(c)). The diffraction rings comprised of continuous spots are also shown in Fig. 3(c), which revealed high angle misorientations of neighboring grains. Besides, the bend contours related to the internal stress were present both in HPT Mg-Ca and Mg-Sr alloys (Fig. 3(b) and (c)). The secondary phase was broken up and distributed more uniformly by HPT processing. Most of the Mg₂Ca phases in the as-cast Mg-Ca alloy existed along the grain boundaries, and the average length is 134 \pm 31 μ m. Some of the Mg₂Ca particles were located within the grains, and the average diameter is 13 \pm 4 μm (Fig. 2(a)). Similarly, most of the Mg₁₇Sr₂ phase of the as-cast Mg-Sr alloy existed within the grain boundaries, and the average length of it is 161 \pm 16 μm . The average size of $Mg_{17}Sr_2$ located within the grains is $11 \pm 2 \mu m$ (Fig. 2(a)). After HPT processing, the Mg₂Ca phase was segmented into fine particles with a size of $6 \pm 2 \mu m$ (Fig. 2(a) and 3(g)) and distributed more uniformly compared with that of the as-cast counterpart. The Mg₁₇Sr2 phase of the HPT Mg-Sr alloy had two kinds of forms with the sizes of 35 \pm 6 μm and 10 \pm 3 μm (Fig. 2(a) and 3(i)), respectively. The size of Mg₂Ca in the as-

extruded Mg–Ca alloy is 13 \pm 4 μm and the size of Mg₁₇Sr2 in the as-extruded Mg–Sr alloy is 17 \pm 7 μm .

XRD spectra of these materials are shown in Fig. 2(b). The stronger diffraction peak of (10 $\bar{1}0$) was detected on the surface perpendicular to the extrusion direction for pure Mg and Mg–Ca alloy after hot extrusion compared with their as-cast counterparts due to texture effects caused by hot extrusion. The intensity of the (0001) reflection was significantly enhanced after these three materials were processed by HPT, indicating that a (0001) $\langle 10\bar{1}0 \rangle$ basal fiber texture was formed, which is also reported by previous studies. ^{22,44,45}

Mechanical properties

The average Vickers hardness of these three materials under different conditions was compared (Fig. 1(d)). The hardness of HPT pure Mg had no significant difference with that of the asextruded pure Mg, both observably higher than that of their as-received counterpart. HPT Mg-Ca alloy had the highest hardness value, which reached 0.91 \pm 0.02 GPa, among all the Mg-Ca alloys. The Mg-Sr alloys processed by hot extrusion and HPT became harder than the as-cast Mg-Sr alloy. Fig. 4 displays the tensile mechanical behaviors of three HPT materials by micro-tensile tests using micro-tensile samples (Fig. 4(a)). Fig. 4(c) shows the corresponding micro-tensile fracture morphology. The stress-strain curves (Fig. 4(a)) show that HPT pure Mg had increased yield stress (YS), ultimate tensile strength (UTS) and elongation, while no typical strain-hardening stage was observed and it was contrary to the situation in which the strain increased accompanying decreased stress. The YS, UTS and elongation of HPT pure Mg were 116.9 \pm 5.6 MPa, 166.9 \pm 6.7 MPa and 29.2 \pm 3.2%, respectively (Fig. 4(b)). The ductile fracture of HPT pure Mg was observed as dimples occurred across the fracture morphology (Fig. 4(c)). The plastic deformation stage was not apparent for HPT Mg-Ca alloy and Mg-Sr alloy, which was attributed to the very high internal

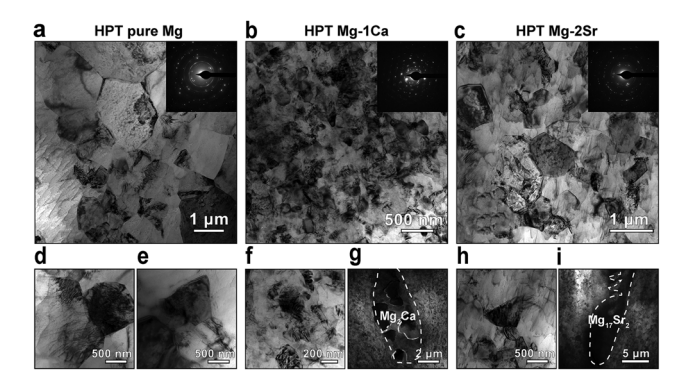


Fig. 3 (a), (b), (c) The representative TEM images of HPT pure Mg, Mg–1Ca and Mg–2Sr alloys, and electron diffraction pattern at the upper right. (d) and (e) The representative higher magnification images of HPT pure Mg. (f) The representative higher magnification images of HPT Mg–1Ca alloy. (g) TEM image of the Mg₂Ca phase of HPT Mg–1Ca alloy. (h) The representative higher magnification images of HPT Mg–2Sr alloy. (i) TEM image of the Mg₁₇Sr₂ phase of HPT Mg–2Sr alloy.

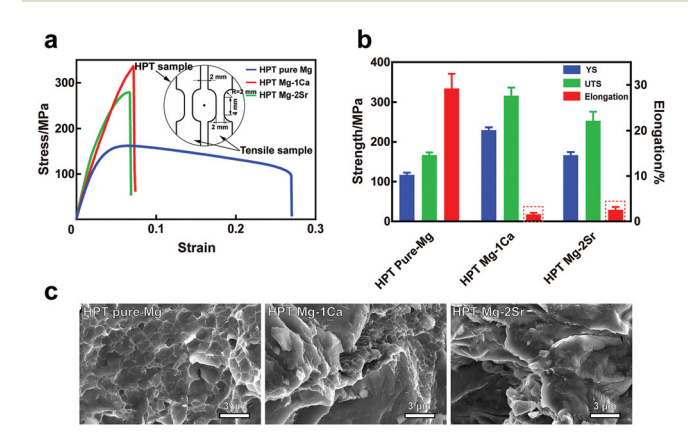


Fig. 4 The tensile mechanical properties of these three HPT materials. (a) Representative stress-strain curves of the materials. (b) Ultimate tensile strength (UTS), yield strength (YS) and elongation of the materials. (c) The representative fracture morphology of these three materials observed by ESEM.

stresses in these samples leading to brittle failure. ⁴⁶ The YS, UTS and elongation of HPT Mg–Ca alloy were 229.4 \pm 7.6 MPa, 315.6 \pm 20.7 MPa and 1.6 \pm 0.3%, respectively (Fig. 4(b)). The fracture morphology of HPT processed Mg–Ca showed both dimples and brittle rupture features (Fig. 4(c)). The YS, UTS and elongation of HPT Mg–Sr alloy were 166.4 \pm 8.1 MPa, 253.3 \pm 23.0 MPa and 2.6 \pm 0.6%, respectively (Fig. 4(b)). The brittle rupture feature of HPT Mg–Sr alloy is also shown in Fig. 4(c).

Biodegradation behavior in vitro

In vitro results of degradation behavior evaluated by immersion tests and hydrogen evolution experiments are shown in Fig. 5. At the initial period of immersion, hydrogen evolution and weight loss ratio of the three types of pure Mg showed no significant difference (Fig. 5(a) and (c)). However, the immersion solution containing HPT pure Mg had a higher pH value compared with that containing the as-cast or as-extruded pure Mg (Fig. 5(b)), indicating the relatively higher degradation rate of HPT pure Mg. After that, a marked increase of hydrogen volume, pH value, and weight loss ratio were observed for HPT pure Mg (Fig. 5(a)–(c)), while these values increased relatively slow for the other two kinds of pure Mg.

According to these results, HPT pure Mg kept degrading at the highest rate compared with its as-cast and as-extruded counterparts. In contrast, the as-cast Mg-Ca alloy and Mg-Sr alloy showed the highest degradation rate among different types of Mg-Ca alloy and Mg-Sr alloy, respectively. No significant difference between the degradation rates of Mg-Ca alloys processed by hot extrusion and HPT was observed during the initial period of immersion. Then the degradation rate of HPT Mg-Ca alloy became lower than that of the asextruded Mg-Ca alloy according to the lower volume of hydrogen and lower pH value of the solution (Fig. 5(d) and (e)). Extrusion and HPT significantly slowed down the degradation rate of the as-received Mg-Sr alloy (Fig. 5(g)-(i)). No significant difference in the degradation rate of these two types of Mg-Sr alloys was observed during the initial period of immersion test. The pH value and the released hydrogen volume of the solution containing HPT Mg-Sr alloy became lower than that containing its as-extruded counterparts in the later period.

The macroscopic appearance of samples after being moved out of Hank's solution is shown in Fig. 6(a), and the surface morphology observed by ESEM is presented in Fig. 6(b). After 24 hours, severe localized corrosion was observed on the sur-

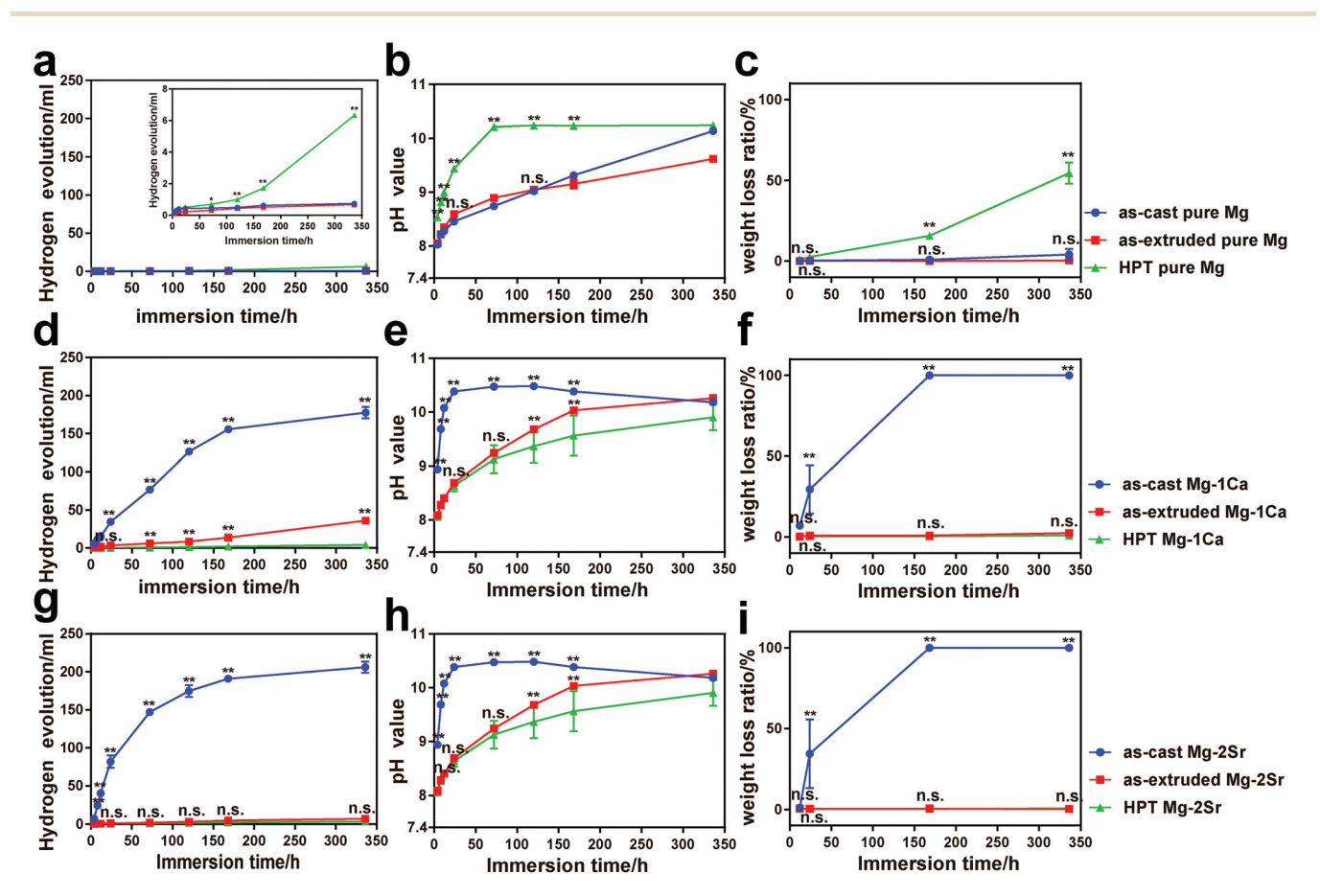


Fig. 5 The *in vitro* biodegradability of these three HPT materials compared with their corresponding as-cast and as-extruded materials. (a), (d), and (g) The hydrogen evolution of pure Mg, Mg–1Ca alloy, and Mg–2Sr alloy with immersion time. (b), (e), and (h) The change of pH value of the solution during the immersion process. (c), (f), and (i) The weight loss ratio of pure Mg, Mg–1Ca alloy, and Mg–2Sr alloy with immersion time.

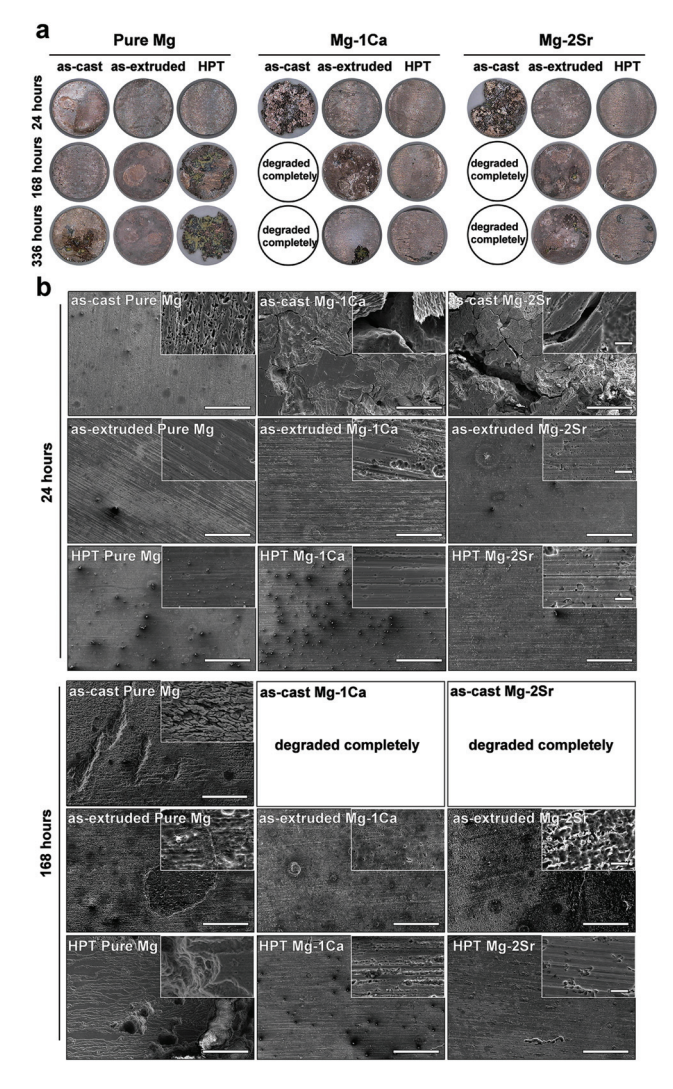


Fig. 6 (a) Macroscopic appearance of samples of the as-cast, as-extruded, and HPT pure Mg, Mg–1Ca alloy and Mg–2Sr alloy after immersion in Hank's solution. (b) Surface morphologies at lower magnification (scale bar = $500~\mu m$) and higher magnification images (placed at the top-right corner of lower magnification image, scale bar = $20~\mu m$) of these materials after immersion in Hank's solution for 24 and 168 hours (the corrosion products were removed).

faces of the as-cast Mg–Ca alloy and Mg–Sr alloy, which preferentially occurred near the grain boundaries. Tiny holes resulting from pitting corrosion were detected on the surface of the as-extruded and HPT samples. After 168 hours of immersion, severe localized corrosion occurred on the surface of HPT pure Mg with the occurrence of corrosion pits. The as-cast Mg–Ca and Mg–Sr alloy were degraded completely, while there was no obvious localized corrosion on the surface of HPT Mg–Ca alloy and Mg–Sr alloy (Fig. 6(b)). After 336 hours of immersion, HPT pure Mg was severely corroded while relatively uniform corrosion was observed on the surface of pure Mg before and after hot extrusion. Localized corrosion began to occur on the surface of Mg–Ca alloy and Mg–Sr alloy processed by hot extrusion and HPT.

Cytotoxicity

Because of the rapid degradation of the as-cast Mg-Ca alloy and Mg-Sr alloy, cell viability can be significantly reduced by the high concentration of the released ions in their extracts. 10,47 Besides, no significant difference in the degradation rate of pure Mg before and after hot extrusion was observed. The cell viability of HPT samples was compared with that of their as-extruded counterparts rather than their as-cast counterparts. The MC3T3 cell viability of all these samples approached or exceeded 80%, indicating good cytocompatibility according to ISO 10993-5 (Fig. 7(a)). No significant difference in MC3T3-E1 cell viability was observed for the HPT samples and their as-extruded counterparts. The extracts of these three materials processed by hot extrusion or HPT had no toxicity to hMSCs and even increased their proliferation (Fig. 7(b)). No significant difference of hMSCs viability of the HPT samples and their as-extruded counterparts was detected after 1 and 3 days of culture. The cell proliferation was excellent for HPT Mg-Ca alloy and Mg-Sr alloy after 5 days of incubation in comparison with that of their as-extruded counterparts, respectively.

In vivo biodegradability

The representative 3D reconstruction models of the implants (Fig. 8(a)) showed that the surfaces of all the three types of implants became rough at week 2 after surgery, and all the implants degraded gradually *in vivo* (Fig. 8(b)). Localized corrosion occurred on the surface of HPT pure Mg after 2 weeks post-operation. Severe localized corrosion was observed for HPT Mg–Ca alloy and Mg–Sr alloy at week 12 post-operation. After 24 weeks of implantation, the HPT pure Mg implant was close to degrading completely, while for the HPT Mg–Ca alloy and Mg–Sr alloy 25% of the volume remained, which was consistent with the sequence of the degradation rate of these three materials *in vitro* (Fig. 5). The calculated corrosion rates of HPT pure Mg, Mg–Ca alloy, and Mg–Sr alloy after 24 weeks' implantation were 0.41 \pm 0.02 mm per year, 0.29 \pm 0.06 mm per year and 0.28 \pm 0.06 mm per year, respectively (Fig. 11(b)).

In vivo biocompatibility

The representative 3D reconstruction models of the bone (green) in the vicinity of the implant (grey) are shown in Fig. 9(a). It was shown that the new bone occurred gradually around the surface of the three materials from week 2 post-operation. At week 24 postimplantation, Giemsa staining (Fig. 9(b)) and HE staining (Fig. 9(c)) of tissue sections showed that all the three types of HPT materials were covered by newformed bone, which suggested the good biocompatibility of these HPT materials. The representative CT images (Fig. 9d) also confirmed this and revealed that although the degrading process was accompanied by the occurrence of a gas cavity around the implant especially during the early period of implantation, the new bone formed gradually in the vicinity of the implant and covered the cavities during the entire healing period.

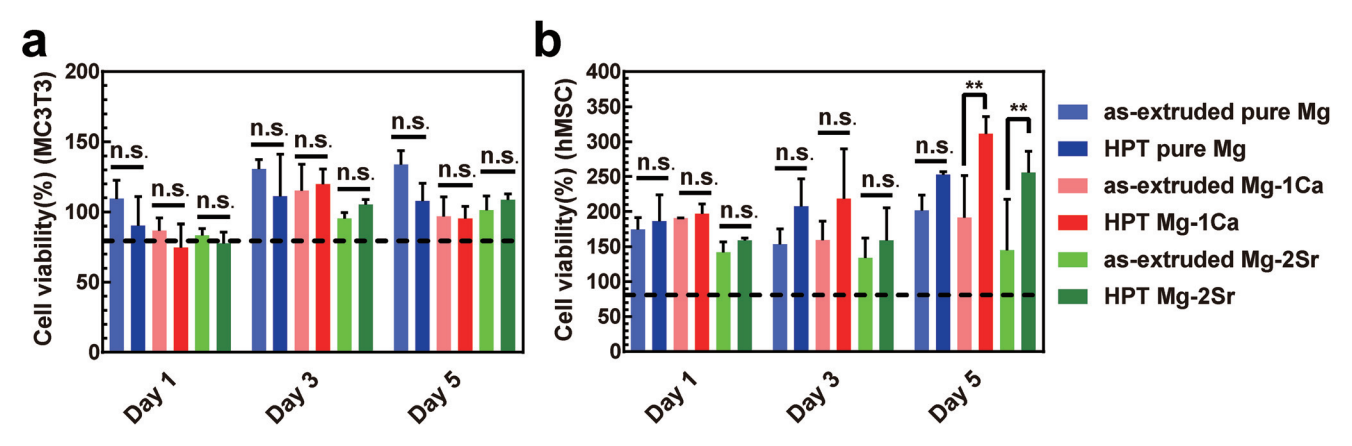


Fig. 7 Cytotoxicity of pure Mg, Mg-1Ca alloy, and Mg-2Sr alloy after hot extrusion and HPT. (a) MC3T3 cell viability of these materials. (b) The hMSC cell viability of these materials.

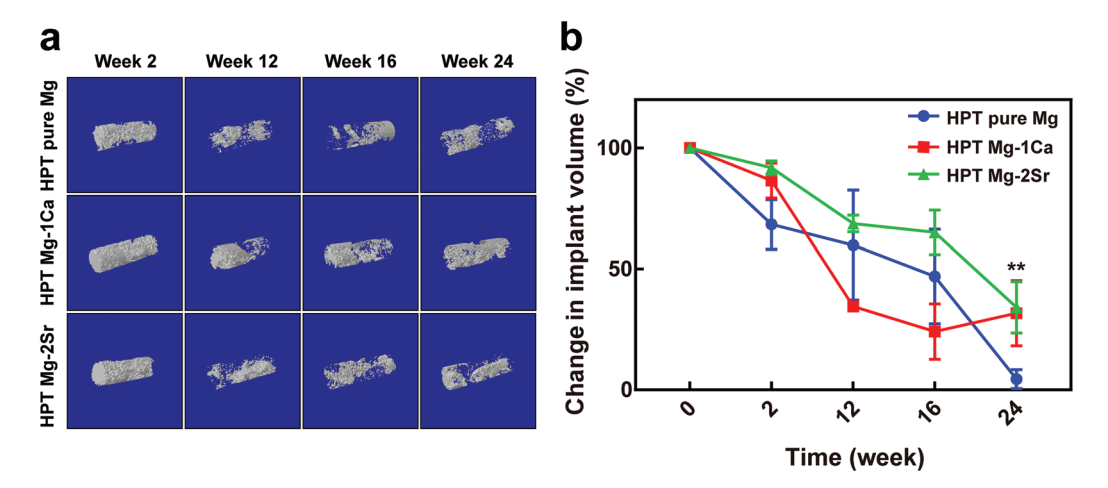


Fig. 8 In vivo degradation behaviors of the three HPT materials. (a) The 3D reconstruction of the implant at 2, 12, 16, and 24 weeks post-implantation. (b) The change of implant volume with implantation time.

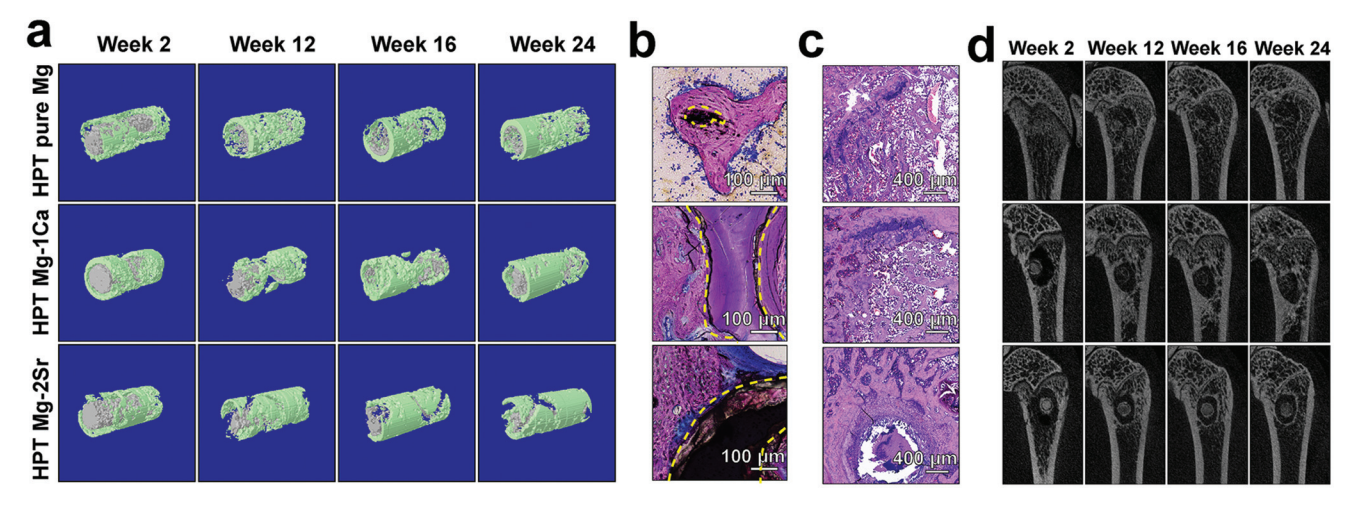


Fig. 9 In vivo biocompatibility of the three HPT materials. (a) The representative 3D reconstruction of the implant (grey) and bone (green) in the vicinity of the implant at 2, 12, 16, and 24 weeks post-implantation. (b) Giemsa staining of undecalcified tissue sections of the implantation site. (c) H–E staining of the decalcified sections of the implantation site. (d) Representative micro-CT images after 2, 12, 16 and 24 weeks of implantation.

Discussion

In our study, ultrafine-grained pure Mg, Mg-Ca alloy, and Mg-Sr alloy were obtained by HPT processing. The bimodal microstructure of HPT pure Mg was revealed in this study and also reported by previous studies. ^{22,23,48-50} Even ten turns of HPT processing did not significantly change the bimodal microstructure character of HPT pure Mg while only a decrease in the area fraction of coarser grains was observed. 45,48 The refinement of grains is attributed to static and dynamic recrystallization.44 During the HPT process, the number of dislocations in the grains gradually increased and dislocations gathered, then the subgrains were formed. This process was confirmed by the gathering of dislocations near the grain boundary in Fig. 3(d). Further deformation leaded to the formation of high-angle grain boundaries (Fig. 3a). At the same time, dynamic crystallization occurred due to the ultra-high strain⁵¹ and elevated temperature of the samples during the process. For HPT Mg-Ca alloy and Mg-Sr alloy, the broken and evenly distributed second phases can hinder dislocation motion, make dislocation pile-up easy, slow down the recovery and retard the migration of recrystallization grain boundaries during the HPT process. The second phases might also be able to provide the nucleation site during the process. Besides, the original grain size of pure Mg is larger than that of Mg-Ca alloy and Mg-Sr alloy. Based on these reasons, the grains in HPT Mg-Ca and Mg-Sr alloys are finer than that in HPT pure Mg. The detailed mechanisms of nanostructure formation during HPT are still not clear²⁰ and need further investigation. This study focused on the influence of HPT on the properties of pure Mg, Mg-Ca alloy, and Mg-Sr alloy, and we will discuss these changes in the following sections.

The change of mechanical properties of pure Mg, Mg–Ca and Mg–Sr alloys by HPT

The mechanical properties of HPT processed materials have attracted a lot of interest among materials science researchers due to their expected increased strength and ductility. In this study, a significant increase in the yield strength of pure Mg was achieved after HPT from ~20 MPa8 to ~117 MPa. HPT increased the ultimate tensile strength from ~80 MPa of the as-cast pure Mg⁸ to ~160 MPa, and this value was also significantly higher than that of hot-extruded magnesium (90-105 MPa¹). The ductility of pure Mg (29.2 \pm 3.2%) after HPT processing increased remarkably compared with that of as-cast Mg $(\sim 13\%^8)$ and as-extruded Mg $(\sim 8.1\%^{52})$. HPT significantly enhanced the mechanical properties of pure Mg, which was related to grain refinement, dislocation density and texture strengthen. 16,22 Besides, the dimples in the fracture surface morphology of HPT pure Mg (Fig. 4) were not smooth but with a convex contour, and the dimensions of these dimples were comparable to the grain size in HPT Mg, indicating grain boundary sliding or rotation also as a deformation mechanism.^{26,53} HPT pure Mg was also reported to process very high elongation, which was attributed to the dominant deformation of grain boundary sliding. 48 Besides, the bimodal

microstructure of HPT pure Mg contributed to the enhanced ductility.^{54,55} If the cracks first occurred in the area where fine grains existed and then propagated onto the interface between the finer grains and larger ones, it can be impeded by the larger grain.⁵⁴

The yield strength of Mg-Ca alloy increased from ~40 MPa to 229.4 MPa by HPT, higher than that of the as-extruded Mg-Ca alloy (~130 MPa⁹), and the ultimate tensile strength exceeds 300 MPa, which is significantly higher than its as-cast counterpart (71.38 MPa⁹) and hot extruded material (239.63 ± 7.21 MPa⁹). For Mg-Sr alloy, the yield strength increased to 116.4 MPa by HPT. Compared with the ultimate tensile strength of the as-cast ($\sim 115 \text{ MPa}^1$) and as-rolled ($\sim 210 \text{ MPa}^{10}$) Mg-Sr alloy, the significant improvement of ultimate tensile strength was achieved by HPT processing to over 250 MPa. The grain refinement and increased dislocation after HPT, as well as the powerful dispersion strengthening related to uniformly distributed second phases contributed to the improvement in the strength of HPT Mg-Ca alloy and Mg-Sr alloy.⁵⁶ However, the ductility of HPT processed Mg-Ca alloy and Mg-Sr alloy is notably low due to the loss of strain-hardening ability,⁵⁷ which is also observed for other HPT Mg alloys without subsequent annealing. 16,46 This is due to the high internal stresses in these materials. Additional annealing can lower the internal stresses and enhance the ductility, 46,58,59 but the processing parameters should be carefully investigated in order to obtain the optimal combination of strength, ductility and even biodegradability.

We have listed the elongation and ultimate tensile strength of HPT magnesium or its alloys that were developed as biomaterials or whose as-received counterparts were previously investigated for biomedical use (Fig. 10). The data of tensile tests of such HPT Mg or its alloys were not very abundant owing to the need for a micro-tensile specimen and an appropriate test machine. This should be considered carefully for the sensitivity of the mechanical properties for HPT processed magnesium to the strain rate, 45 which is shown by the data points marked with red color in Fig. 10. The higher strain rate used in our study during the tensile test may partially cause the high strength and low ductility of HPT materials. This strain rate sensitivity results from the contributions of grain boundary sliding to the overall deformation mechanism. 48 A pronounced increase of elongation could be achieved when the strain rate decreased, because the grain sliding plays a crucial part in the deformation. 48,49,60,61 It can be speculated that the elongation of the ultrafine-grained pure Mg, Mg-Ca alloy and Mg-Sr alloy in our study could be improved at a lower strain rate. It can be noticed that the HPT Mg-Ca alloy in this study had high tensile strength among the HPT magnesium materials (Fig. 10). The yield strength and tensile strength are also higher than those of the commercial extruded AZ31 alloy and WE43 alloy. 62,63 The ultimate tensile strength of HPT Mg-Ca alloy is comparable to that of the commercially used MAGNEZIX-MgYREZr alloy which is applied in hallux valgus surgery. 64,65 However, the yield strength $(R_{p0.2})$ of HPT Mg-Ca alloy (230 MPa) is lower than that of MAGNEZIX-MgYREZr

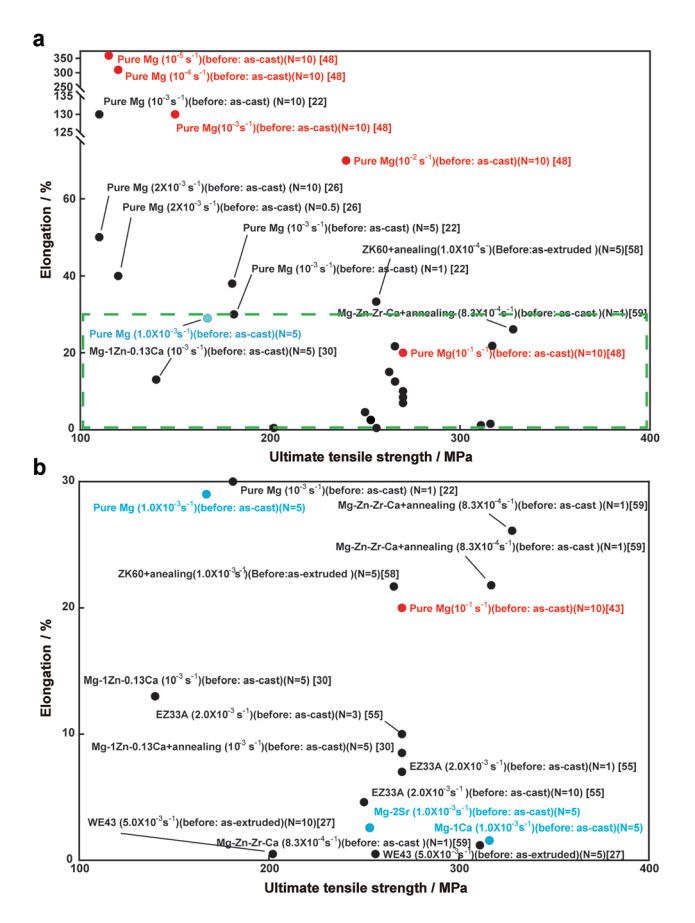


Fig. 10 Elongation and ultimate tensile strength of HPT processed Mg or its alloys that may have potential for medical use according to the results of previous tensile tests at room temperature. The strain rate of tensile tests, the original state of the materials and the turns (N) during HPT processing are listed in brackets.

alloy (250 MPa). Moreover, the low ductility of HPT Mg-Ca alloy is not desirable. The significant improvement of the strength of Mg-Ca alloy by HPT will have the potential to broaden its applications if its low ductility is modified.

To sum up, HPT processing is an effective way to improve the strength and ductility of pure Mg simultaneously, while HPT processing leads to an increase in strength but a brittle behavior of Mg–Ca and Mg–Sr alloys, which needs to be modified by additional annealing.

The change of degradation rate and behavior of pure Mg, Mg-Ca and Mg-Sr alloys after HPT

The effect of HPT processing on the corrosion behavior of magnesium and its alloys in simulated body fluid is controversial according to the previous reports, as shown in Fig. 11(a). Fig. 11(a) shows the change of corrosion rate of Mg and its alloys in simulated body fluid after HPT according to the results of electrochemical tests and immersion tests. Some reports showed that HPT had no significant influence on the corrosion resistance of pure Mg or Mg alloys.²⁴ For example, Donya Ahmadkhaniha *et al.*²² reported that there is no signifi-

cant improvement of the corrosion resistance of HPT pure Mg compared with the as-cast pure Mg. Claudio L. P. Silva et al. 25 also showed that HPT had no discernible influence on the corrosion performance of AZ31, AZ91 and ZK60 in a 3.5% NaCl solution (Fig. 11(a)). There are also many pieces of evidence which indicated that HPT could significantly improve the corrosion resistance of pure Mg,^{24,25} Mg–Zn–Ca alloy⁶⁶ and WE43 alloy²⁸ in 3.5% NaCl solution, SBF, and 0.9% NaCl solution, respectively. One of the reasons for the improvement is believed to be the uniform distribution of the second phase of Mg alloys or the impurities of pure Mg, avoiding severe localized corrosion and causing homogeneous corrosion. 37,66 Besides, it was thought that the increase of grain boundary density of pure Mg and its alloys could reduce the mismatch and disorder between the material surface and oxide layer, which can further protect the matrix.⁶⁷ Besides, the surface with (0001) basal texture was confirmed to have improved corrosion resistance. 68,69 However, HPT was reported to decrease the corrosion resistance of pure titanium.⁷⁰ AZ31 alloy with a significantly refined microstructure was more susceptible to corrosion in 3.5% NaCl electrolyte compared with coarsegrained materials, which resulted from increased dislocation densities.⁷¹ All of these discrepancies may come from the different final microstructures, dislocation density, residual stress, testing methods and the corrosion mechanism of the material. 72,73 The effect of HPT on the corrosion behavior of Mg or its alloys needs to be specifically analyzed.

The immersion test results in this study (Fig. 5 and 6) confirmed the different effects of HPT on the degradation behavior of magnesium materials, showing that HPT enhanced the corrosion resistance of Mg-Ca alloy and Mg-Sr alloy, and accelerated the degradation of pure Mg in vitro. For HPT pure Mg, a higher degradation rate and pitting corrosion were observed, although the ultrafine-grained microstructure and basal texture were confirmed. It can be speculated that the bimodal microstructure might be the reason for this decreased corrosion resistance.⁷⁴ The larger grains nearly without dislocations and finer grains with dislocations may have different potential and can form galvanic corrosion, leading to the pitting corrosion. For Mg-Ca alloy and Mg-Sr alloy, the size and distribution of the second phase can significantly influence the degradation behavior according to this study and the previous report.⁷⁵ There was no obvious difference between HPT Mg-Ca or Mg-Sr alloy and their corresponding asextruded counterparts, which resulted from significant modification of the size and distribution of Mg2Ca and Mg17Sr2 phases by HPT and hot extrusion. The second phase and the α-Mg matrix formed a galvanic cell with a significant potential difference.⁷⁶ The Mg₂Ca phase was observed to act as an anode in the Mg-Mg₂Ca galvanic pattern, 75,77 while the Mg₁₇Sr₂ phases acted as a cathode in the Mg-Mg₁₇Sr₂ galvanic pattern. 10,78 Before HPT processing, Mg2Ca and Mg17Sr2 phases were coarse and distributed mainly along the grain boundaries, resulting in severe intergranular corrosion. The size of the Mg₂Ca and Mg₁₇Sr₂ of HPT Mg-Ca alloy and Mg-Sr alloy was decreased (Fig. 3) and the distribution became more

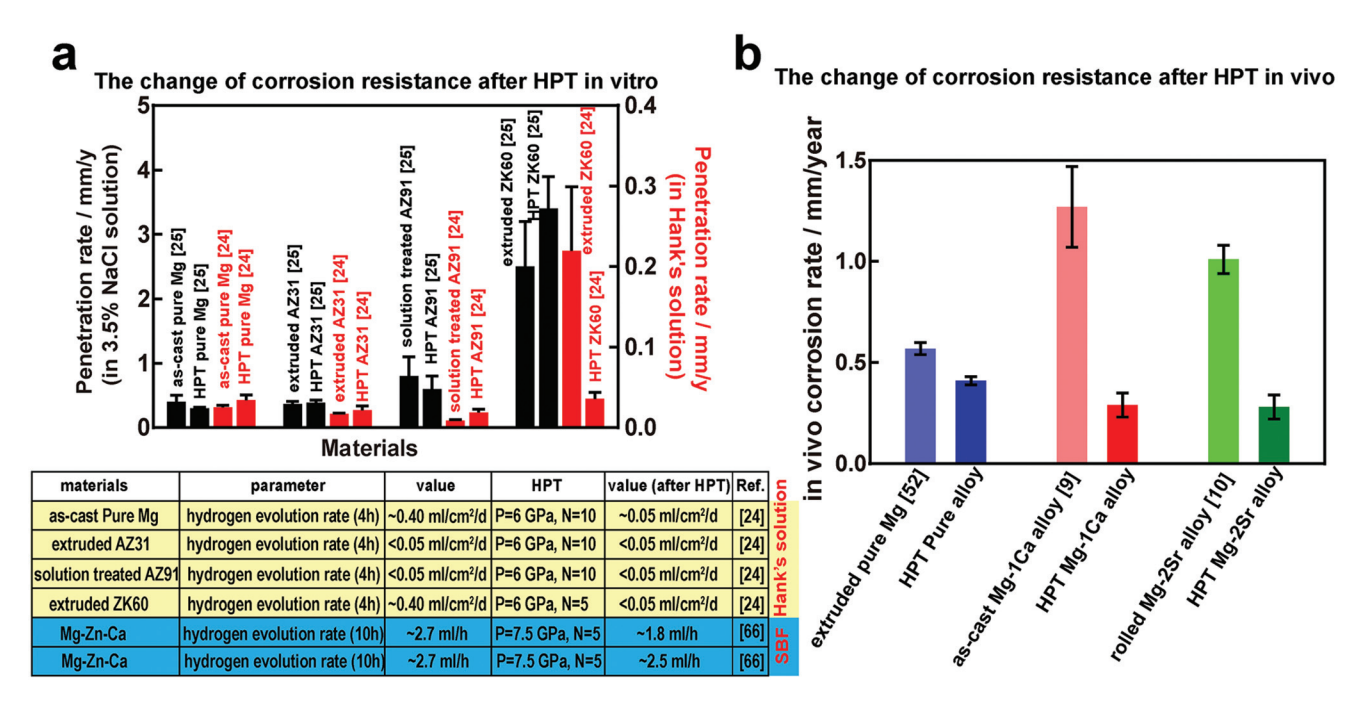


Fig. 11 The effect of HPT on the corrosion resistance of Mg and its alloys (a) in vitro according to previous results of electrochemical tests and immersion tests, and (b) in vivo. P is the pressure, and N is the number of turns during HPT.

uniform (Fig. 2), so micro galvanic corrosion could occur across the whole materials' surface resulting in uniform corrosion. Besides, the ultrafine-grained microstructure of HPT Mg–Ca alloy and Mg–Sr alloy promoted the formation of a more uniform surface corrosion layer, providing efficient protection of the matrix.⁷⁵

Fig. 11(b) shows the comparison of in vivo corrosion resistance of pure Mg, Mg-Ca alloy and Mg-Sr alloy after HPT and other conventional plastic deformation. Although HPT increased the degradation rate of pure Mg in vitro, the degradation rate is still a little lower than that of hot extruded high pure Mg in vivo. 52 Compared with the in vivo degradation behavior of the as-cast Mg-Ca alloy, which remained lower than 4% volume after 3 months, the in vivo degradation rate of the HPT Mg-Ca alloy is relatively lower. Rolled Mg-Sr alloy had lower than 50% volume after 4 weeks, 10 indicating that the in vivo degradation rate of HPT Mg-Sr alloy is relatively lower. The comparison of the calculated in vivo corrosion rate also confirms this (Fig. 11(b)). Besides, the degradation rates of these three HPT materials were lower than that of the RE-containing magnesium alloys within the bone environment.⁷⁹ The relatively lower degradation rate is beneficial for keeping the biocompatibility and bioactivity, as well as maintaining the mechanical integrity of the materials in the physiological environment. However, it is worth noting that the animal model and implantation sites in these studies are not entirely consistent, so further investigations are needed. The lower degradation of these HPT materials might also be attributed to the ultrafine-grained microstructure, which can regulate the degree of cell attachment and rate of growth by interacting with proteins. 80 The exact underlying mechanism also requires further investigation. In conclusion, HPT is shown to be a powerful way to slow down the degradation rate of pure Mg, Mg–Ca alloy and Mg–Sr alloy *in vivo*.

The good biocompatibility of HPT pure Mg, Mg-Ca and Mg-Sr alloys

It is believed that materials with fine-grained microstructures can enhance cell adhesion and activities. 80-82 For example, Maryam Tabrizian et al. 80,82 showed that osteoblast adhesion and proliferation rate were notably improved on the surface of HPT titanium compared with those on titanium with coarse grain due to the regulation of the activity of proteins existing in the extracellular matrix by the nanostructured features of the materials. However, biodegradable magnesium has a dynamically changing surface in the physiological environment which is different from titanium or its alloys, and the influence factors which can change the cell behaviors become more complicated. There are only several studies focusing on the biocompatibility of HPT Mg and its alloys in vitro. Good cytocompatibility of HPT pure Mg, AZ31, AZ91, and ZK60 alloys was reported previously.26,82 The cell viability tests in this study were conducted using the extracts containing the released ions of the materials. It was shown that the extracts of these three HPT magnesium materials after HPT had good cell compatibility for MC3T3 cells and hMSCs, which even could promote the proliferation of these cells.

Commercial pure Mg screws were implanted as craniofacial bone screws in a rabbit mandible and bone remodeling occurred around the screws.⁸³ Other investigations also confirmed the good biocompatibility of pure Mg and its active effect on bone formation.^{7,52} HPT pure Mg in our research

Table 2 Comparison of properties of ECAP and HPT Mg materials

Materials	Grain size (μm)	YS (MPa)	UTS (MPa)	Elongation (%)	<i>In vivo</i> degradation rate (mm per year)
HPT pure Mg	$1.8 \pm 0.5/0.59 \pm 0.12$	116.9 ± 5.6	166.9 ± 6.7	29.2% ± 3.2%	0.41 ± 0.02
ECAP pure Mg	~2/~0.8	~30	~100	~12%	~0.55
HPT Mg-1Ca	0.17 ± 0.52	229.4 ± 7.6	315.6 ± 20.7	$1.6\% \pm 0.3\%$	0.29 ± 0.06
ECAP Mg-1Ca	~1	~125	~200	~7%	~0.24
HPT Mg-2Sr	0.72 ± 0.18	166.4 ± 8.1	253.3 ± 23.0	$2.6\% \pm 0.6\%$	0.28 ± 0.06
ECAP Mg-2Sr	~2	~110	~170	~8%	~0.30
· ·					

also showed good in vivo biocompatibility with the new bone formed around it. Mg-Ca alloy pins were implanted into rabbit femoral shafts9 and the results showed that Mg-Ca alloy had good biocompatibility by the high activity of osteoblast and osteocytes around the alloy pins. As expected, the ultrafine-grained Mg-Ca alloy in this study also showed good biocompatibility in vivo, with gradual new bone formation around the implant (Fig. 9(a)-(c)). It was shown that the destroyed bone (gravities in Fig. 9(d)) was replaced by new bone within the implantation period around the Mg-Ca alloy implant. Mg-Sr alloy was previously implanted into a predrilled bone tunnel in the femur along the axis of the shaft from the distal femur of C57BL/6 mice. 10 Enhanced bone mineral density and thicker cortical bone were observed around the experimental implants. Also, the good biocompatibility of the Mg-Sr alloy after HPT was revealed in this study. The ions released from the materials processed by conventional procedures and from their HPT counterparts are same due to the same composition of these materials, and the degradation rates of these materials in vivo are all well tolerated by the physiological environment. Besides, the ultrafinegrained surface did not compromise the good compatibility of magnesium materials.

HPT processing as an alternative avenue for improving the comprehensive performance of biodegradable magnesium

The challenges for biodegradable Mg materials are to obtain appropriate biodegradable behavior, to maintain mechanical integrity during the early implantation period and to maintain biosafety during their degradation processing.¹ Thus far, the major two methods for enhancing the properties of biodegradable Mg and its alloys are surface modification^{84,85} and alloying.¹,4,86</sup> In this study, we used HPT to refine the microstructure of biodegradable Mg and its alloys and to enhance their properties. In comparison with alloying and surface modification, HPT avoids the issues of the potentially toxic effects of alloying elements and the uncontrollable degradation when the surface-modified layer breaks down. Once defects arise within the coatings, the solution will rapidly permeate, resulting in the rapid corrosion of Mg alloys by pitting corrosion.

Another severe plastic deformation process, equal channel angular pressing (ECAP), was also used to refine the microstructure of pure Mg, Mg–Ca alloy and Mg–Sr alloy.⁸⁷ We compared the properties of the three HPT materials with their

ECAP counterparts (Table 2). As shown in Table 2, HPT is confirmed to be a more effective way to reduce the grain size of pure Mg, Mg–Ca alloy and Mg–Sr alloy compared with ECAP. The mechanical strength of the three HPT materials is higher than that of their ECAP counterparts, but the ductility of HPT Mg–Ca alloy and Mg–Sr alloy is lower. The *in vivo* degradation rate of HPT samples had no distinct difference from that of their ECAP samples. HPT and ECAP, as two kinds of severe plastic deformation processes, may become alternative ways of development of biodegradable materials.

The most significant limitation of HPT is its restricted sample size, which needs to be solved by the further development of HPT technology. HPT samples on such a small scale are not suitable for the fabrication of screw and plate in humans. Another limitation is the low ductility of HPT Mg–Ca and Mg–Sr alloys in this study, and this needs to be enhanced by subsequent annealing. HPT Mg–Ca and Mg–Sr alloys with additional annealing have the possibility to be fabricated into barrier membranes with the thickness of tens of micrometers for guided bone regeneration (GBR). The membranes were used to prevent in-growth of soft tissue on the bone defect and promote the bone tissue regeneration. Besides, the degradable membranes can avoid second surgery for their removal. This is intriguing for further investigations.

Conclusions

HPT can significantly modify the microstructure of biodegradable pure Mg, Mg-Ca alloy and Mg-Sr alloy. The bimodal ultrafine-grained microstructures were produced in pure Mg after HPT. HPT simultaneously improved the mechanical strength and ductility of pure Mg compared with as-cast and extruded counterparts. Although HPT increased the in vitro degradation rate of HPT pure Mg, the cell viability tests and the animal tests confirmed the good biocompatibility of HPT pure Mg. HPT Mg-Ca alloy and Mg-Sr alloy obtained a homogeneous ultrafine-grained microstructure and had significantly higher mechanical strength than the conventional procedure processed counterparts. Relatively low degradation rate, good biocompatibility and the ability to promote the bone formation of HPT Mg-Ca alloy and Mg-Sr alloy were revealed. The results of our study showed that HPT is an alternative way to develop biodegradable Mg and its alloys.

Conflicts of interest

The authors declare no conflict of interest.

Acknowledgements

This work was supported by the National Natural Science Foundation of China (Grant No. 51871004), and NSFC/RGC Joint Research Scheme (Grant No. 51661165014). The authors (RZV and OBK) would like to acknowledge the partial financial support in the framework of the RFBR project 20-58-S52001 MHT a.

Notes and references

- 1 Y. F. Zheng, X. N. Gu and F. Witte, Biodegradable metals, *Mater. Sci. Eng.*, R, 2014, 77, 1–34.
- 2 D. Zhao, F. Witte, F. Lu, J. Wang, J. Li and L. Qin, Current status on clinical applications of magnesium-based orthopaedic implants: A review from clinical translational perspective, *Biomaterials*, 2017, 112, 287–302.
- 3 N. Li and Y. Zheng, Novel Magnesium Alloys Developed for Biomedical Application: A Review, *J. Mater. Sci. Technol.*, 2013, 29(6), 489–502.
- 4 Y. Liu, Y. F. Zheng, X. H. Chen, J. A. Yang, H. B. Pan, D. F. Chen, L. N. Wang, J. L. Zhang, D. H. Zhu, S. L. Wu, K. W. K. Yeung, R. C. Zeng, Y. Han and S. K. Guan, Fundamental Theory of Biodegradable Metals-Definition, Criteria, and Design, *Adv. Funct. Mater.*, 2019, 29(18), 21.
- 5 J. H. F. de Baaij, J. G. J. Hoenderop and R. J. M. Bindels, Magnesium in man: implications for health and disease, *Physiol. Rev.*, 2015, **95**(1), 1–46.
- 6 M. P. Staiger, A. M. Pietak, J. Huadmai and G. Dias, Magnesium and its alloys as orthopedic biomaterials: A review, *Biomaterials*, 2006, 27(9), 1728–1734.
- 7 Y. Zhang, J. Xu, Y. C. Ruan, M. K. Yu, M. O'Laughlin, H. Wise, D. Chen, L. Tian, D. Shi, J. Wang, S. Chen, J. Q. Feng, D. H. K. Chow, X. Xie, L. Zheng, L. Huang, S. Huang, K. Leung, N. Lu, L. Zhao, H. Li, D. Zhao, X. Guo, K. Chan, F. Witte, H. C. Chan, Y. Zheng and L. Qin, Implant-derived magnesium induces local neuronal production of CGRP to improve bone-fracture healing in rats, *Nat. Med.*, 2016, 22(10), 1160–1169.
- 8 X. Gu, Y. Zheng, Y. Cheng, S. Zhong and T. Xi, In vitro corrosion and biocompatibility of binary magnesium alloys, *Biomaterials*, 2009, **30**(4), 484–498.
- 9 Z. Li, X. Gu, S. Lou and Y. Zheng, The development of binary Mg–Ca alloys for use as biodegradable materials within bone, *Biomaterials*, 2008, **29**(10), 1329–1344.
- 10 X. N. Gu, X. H. Xie, N. Li, Y. F. Zheng and L. Qin, In vitro and in vivo studies on a Mg–Sr binary alloy system developed as a new kind of biodegradable metal, *Acta Biomater.*, 2012, **8**(6), 2360–2374.

11 P. J. Marie, The calcium-sensing receptor in bone cells: A potential therapeutic target in osteoporosis, *Bone*, 2010, 46(3), 571–576.

- 12 S. Maeno, Y. Niki, H. Matsumoto, H. Morioka, T. Yatabe, A. Funayama, Y. Toyama, T. Taguchi and J. Tanaka, The effect of calcium ion concentration on osteoblast viability, proliferation and differentiation in monolayer and 3D culture, *Biomaterials*, 2005, **26**(23), 4847–4855.
- 13 A. Hoppe, N. S. Gueldal and A. R. Boccaccini, A review of the biological response to ionic dissolution products from bioactive glasses and glass-ceramics, *Biomaterials*, 2011, 32(11), 2757–2774.
- 14 P. J. Meunier, D. O. Slosman, P. D. Delmas, J. L. Sebert, M. L. Brandi, C. Albanese, R. Lorenc, S. Pors-Nielsen, M. C. de Vernejoul, A. Roces and J. Y. Reginster, Strontium ranelate: Dose-dependent effects in established postmenopausal vertebral osteoporosis A 2-year randomized placebo controlled trial, *J. Clin. Endocrinol. Metab.*, 2002, 87(5), 2060–2066.
- 15 A. P. Zhilyaev and T. G. Langdon, Using high-pressure torsion for metal processing: Fundamentals and applications, *Prog. Mater. Sci.*, 2008, 53(6), 893–979.
- 16 R. B. Figueiredo and T. G. Langdon, Processing Magnesium and Its Alloys by High-Pressure Torsion: An Overview, *Adv. Eng. Mater.*, 2019, **21**(1), 1801039.
- 17 Q. Wu, S. Zhu, L. Wang, Q. Liu, G. Yue, J. Wang and S. Guan, The microstructure and properties of cyclic extrusion compression treated Mg-Zn-Y-Nd alloy for vascular stent application, *J. Mech. Behav. Biomed. Mater.*, 2012, 8, 1–7.
- 18 A. Galiyev, O. Sitdikov and R. Kaibyshev, Deformation behavior and controlling mechanisms for plastic flow of magnesium and magnesium alloy, *Mater. Trans.*, 2003, 44(4), 426–435.
- 19 C. C. Koch, T. G. Langdon and E. J. Lavernia, Bulk Nanostructured Materials, *Metall. Mater. Trans. A*, 2017, 48(11), 5181–5199.
- 20 R. Z. Valiev, R. K. Islamgaliev and I. V. Alexandrov, Bulk nanostructured materials from severe plastic deformation, *Prog. Mater. Sci.*, 2000, 45(2), 103–189.
- 21 M. Kai, Z. Horita and T. G. Langdon, Developing grain refinement and superplasticity in a magnesium alloy processed by high-pressure torsion, *Mater. Sci. Eng.*, *A*, 2008, 488(1–2), 117–124.
- 22 D. Ahmadkhaniha, Y. Huang, M. Jaskari, A. Jarvenpaa, M. H. Sohi, C. Zanella, L. P. Karjalainen and T. G. Langdon, Effect of high-pressure torsion on microstructure, mechanical properties and corrosion resistance of cast pure Mg, J. Mater. Sci., 2018, 53(24), 16585–16597.
- 23 K. Edalati, A. Yamamoto, Z. Horita and T. Ishihara, High-pressure torsion of pure magnesium: Evolution of mechanical properties, microstructures and hydrogen storage capacity with equivalent strain, *Scr. Mater.*, 2011, **64**(9), 880–883.
- 24 D. R. Lopes, C. L. P. Silva, R. B. Soares, P. H. R. Pereira, A. C. Oliveira, R. B. Figueiredo, T. G. Langdon and

- V. F. C. Lins, Cytotoxicity and Corrosion Behavior of Magnesium and Magnesium Alloys in Hank's Solution after Processing by High-Pressure Torsion, *Adv. Eng. Mater.*, 2019, 21(8), 1900391.
- 25 C. L. P. Silva, R. B. Soares, P. H. R. Pereira, R. B. Figueiredo, V. F. C. Lins and T. G. Langdon, The Effect of High-Pressure Torsion on Microstructure, Hardness and Corrosion Behavior for Pure Magnesium and Different Magnesium Alloys, Adv. Eng. Mater., 2019, 21(3), 9.
- 26 C. L. P. Silva, A. C. Oliveira, C. G. F. Costa, R. B. Figueiredo, M. d. F. Leite, M. M. Pereira, V. F. C. Lins and T. G. Langdon, Effect of severe plastic deformation on the biocompatibility and corrosion rate of pure magnesium, *J. Mater. Sci.*, 2017, 52(10), 5992–6003.
- 27 D. X. Liu, X. Pang, D. L. Li, C. G. Guo, J. Wongsa-Ngam, T. G. Langdon and M. A. Meyers, Microstructural Evolution and Properties of a Hot Extruded and HPT-Processed Resorbable Magnesium WE43 Alloy, *Adv. Eng. Mater.*, 2017, 19(3), 1700723.
- 28 E. A. Lukyanova, N. S. Martynenko, V. N. Serebryany, A. N. Belyakov, L. L. Rokhlin, S. V. Dobatkin and Y. Z. Estrin, Structure and Mechanical and Corrosion Properties of a Magnesium Mg-Y-Nd-Zr Alloy after High Pressure Torsion, *Russ. Metall.*, 2017, (11), 912–921.
- 29 F. Meng, J. M. Rosalie, A. Singh, H. Somekawa and K. Tsuchiya, Ultrafine grain formation in Mg-Zn alloy by in situ precipitation during high-pressure torsion, *Scr. Mater.*, 2014, 78–79, 57–60.
- 30 O. B. Kulyasova, R. K. Islamgaliev and R. Z. Valiev, Microstructure and Mechanical Properties of Ultrafine-Grained Mg-Zn-Ca Alloy, *Defect Diffus. Forum*, 2017, **381**, 39–43.
- 31 J. Horky, A. Ghaffar, K. Werbach, B. Mingler, S. Pogatscher, R. Schaeublin, D. Setman, P. J. Uggowitzer, J. F. Loeffler and M. J. Zehetbauer, Exceptional Strengthening of Biodegradable Mg-Zn-Ca Alloys through High Pressure Torsion and Subsequent Heat Treatment, *Materials*, 2019, 12(15), 2460.
- 32 Q. Su, J. Xu, Y. Li, J. I. Yoon, D. Shan, B. Guo and H. S. Kim, Microstructural Evolution and Mechanical Properties in Superlight Mg-Li Alloy Processed by High-Pressure Torsion, *Materials*, 2018, **11**(4), 598.
- 33 Y. I. Bourezg, H. Azzeddine, T. Baudin, A.-L. Helbert, Y. Huang, D. Bradai and T. G. Langdon, Texture and microhardness of Mg-Rare Earth (Nd and Ce) alloys processed by high-pressure torsion, *Mater. Sci. Eng.*, A, 2018, 724, 477–485.
- 34 A. Hanna, H. Azzeddine, R. Lachhab, T. Baudin, A.-L. Helbert, F. Brisset, Y. Huang, D. Bradai and T. G. Langdon, Evaluating the textural and mechanical properties of an Mg-Dy alloy processed by high-pressure torsion, *J. Alloys Compd.*, 2019, 778, 61–71.
- 35 W. T. Sun, X. G. Qiao, M. Y. Zheng, X. J. Zhao, H. W. Chen, N. Gao and M. J. Starink, Achieving ultra-high hardness of nanostructured Mg-8.2Gd-3.2Y-1.0Zn-0.4Zr alloy produced by a combination of high pressure torsion and ageing treatment, *Scr. Mater.*, 2018, **155**, 21–25.

36 R. Kocich, L. Kuncicka, P. Kral and T. C. Lowe, Texture, deformation twinning and hardening in a newly developed Mg-Dy-Al-Zn-Zr alloy processed with high pressure torsion, *Mater. Des.*, 2016, **90**, 1092–1099.

- 37 C. Z. Zhang, S. J. Zhu, L. G. Wang, R. M. Guo, G. C. Yue and S. K. Guan, Microstructures and degradation mechanism in simulated body fluid of biomedical Mg-Zn-Ca alloy processed by high pressure torsion, *Mater. Des.*, 2016, 96, 54–62.
- 38 W. C. Oliver and G. M. Pharr, An Improved Technique For Determining Hardness And Elastic-Modulus Using Load And Displacement Sensing Indentation Experiments, *J. Mater. Res.*, 1992, 7(6), 1564–1583.
- 39 F. Witte, J. Fischer, J. Nellesen, C. Vogt, J. Vogt, T. Donath and F. Beckmann, In vivo corrosion and corrosion protection of magnesium alloy LAE442, *Acta Biomater.*, 2010, **6**(5), 1792–1799.
- 40 T. G. Langdon, Twenty-five years of ultrafine-grained materials: Achieving exceptional properties through grain refinement, *Acta Mater.*, 2013, **61**(19), 7035–7059.
- 41 M. Kawasaki, R. B. Figueiredo and T. G. Langdon, An investigation of hardness homogeneity throughout disks processed by high-pressure torsion, *Acta Mater.*, 2011, 59(1), 308–316.
- 42 F. A. Mohamed and S. S. Dheda, On the minimum grain size obtainable by high-pressure torsion, *Mater. Sci. Eng.*, *A*, 2012, **558**, 59–63.
- 43 C. L. P. Silva, R. B. Soares, P. H. R. Pereira, R. B. Figueiredo, V. F. C. Lins and T. G. Langdon, The Effect of High-Pressure Torsion on Microstructure, Hardness and Corrosion Behavior for Pure Magnesium and Different Magnesium Alloys, *Adv. Eng. Mater.*, 2019, 21(3), 1801081.
- 44 J. Cizek, I. Prochazka, B. Smola, I. Stulikova, R. Kuzel, Z. Matej, V. Cherkaska, R. K. Islamgaliev and O. Kulyasova, Microstructure and thermal stability of ultra fine grained Mg-based alloys prepared by high-pressure torsion, *Mater. Sci. Eng.*, A, 2007, 462(1-2), 121-126.
- 45 R. B. Figueiredo, S. Sabbaghianrad and T. G. Langdon, The effect of high-pressure torsion on the microstructure and properties of magnesium, in *7th International Conference on Nanomaterials by Severe Plastic Deformation*, ed. X. Liao and Y. Estrin, 2017.
- 46 O. B. Kulyasova, R. K. Islamgaliev, E. V. Parfenov, Y. F. Zheng and R. Z. Valiev, Microstructure, mechanical and corrosion properties of ultrafine-grained Mg-2%Sr alloy, *IOP Conf. Ser.: Mater. Sci. Eng.*, 2018, 380, 012014.
- 47 F. Witte, N. Hort, C. Vogt, S. Cohen, K. U. Kainer, R. Willumeit and F. Feyerabend, Degradable biomaterials based on magnesium corrosion, *Curr. Opin. Solid State Mater. Sci.*, 2008, 12(5-6), 63-72.
- 48 R. B. Figueiredo, S. Sabbaghianrad, A. Giwa, J. R. Greer and T. G. Langdon, Evidence for exceptional low temperature ductility in polycrystalline magnesium processed by severe plastic deformation, *Acta Mater.*, 2017, 122, 322–331.
- 49 R. B. Figueiredo, F. S. J. Poggiali, C. L. P. Silva, P. R. Cetlin and T. G. Langdon, The influence of grain size and strain

rate on the mechanical behavior of pure magnesium, *J. Mater. Sci.*, 2016, 51(6), 3013–3024.

- 50 B. J. Bonarski, E. Schafler, B. Mingler, W. Skrotzki, B. Mikulowski and M. J. Zehetbauer, Texture evolution of Mg during high-pressure torsion, *J. Mater. Sci.*, 2008, 43(23–24), 7513–7518.
- 51 R. B. Figueiredo, P. R. Cetlin and T. G. Langdon, Using finite element modeling to examine the flow processes in quasi-constrained high-pressure torsion, *Mater. Sci. Eng., A*, 2011, 528(28), 8198–8204.
- 52 P. Han, P. Cheng, S. Zhang, C. Zhao, J. Ni, Y. Zhang, W. Zhong, P. Hou, X. Zhang, Y. Zheng and Y. Chai, In vitro and in vivo studies on the degradation of high-purity Mg (99.99 wt%) screw with femoral intracondylar fractured rabbit model, *Biomaterials*, 2015, **64**, 57–69.
- 53 Y. Wan, S. Xu, C. Liu, Y. Gao, S. Jiang and Z. Chen, Enhanced strength and corrosion resistance of Mg-Gd-Y-Zr alloy with ultrafine grains, *Mater. Lett.*, 2018, **213**, 274–277.
- 54 Z. Lee, V. Radmilovic, B. Ahn, E. J. Lavernia and S. R. Nutt, Tensile Deformation and Fracture Mechanism of Bulk Bimodal Ultrafine-Grained Al-Mg Alloy, *Metall. Mater. Trans. A*, 2010, 41(4), 795–801.
- 55 K. Bryla, J. Morgiel, M. Faryna, K. Edalati and Z. Horita, Effect of high-pressure torsion on grain refinement, strength enhancement and uniform ductility of EZ magnesium alloy, *Mater. Lett.*, 2018, 212, 323–326.
- 56 M. V. Markushev, E. V. Avtokratova, S. V. Krymskiy and O. S. Sitdikov, Effect of precipitates on nanostructuring and strengthening of high-strength aluminum alloys under high pressure torsion, *J. Alloys Compd.*, 2018, 743, 773–779.
- 57 J. G. Sevillano, I. O. Arizcorreta and L. P. Kubin, Intrinsic size effects in plasticity by dislocation glide, *Mater. Sci. Eng.*, *A*, 2001, **309**, 393–405.
- 58 S. A. Torbati-Sarraf, S. Sabbaghianrad and T. G. Langdon, Using Post-Deformation Annealing to Optimize the Properties of a ZK60 Magnesium Alloy Processed by High-Pressure Torsion, *Adv. Eng. Mater.*, 2018, **20**(2), 1700703.
- 59 R. Zheng, T. Bhattacharjee, A. Shibata, T. Sasaki, K. Hono, M. Joshi and N. Tsuji, Simultaneously enhanced strength and ductility of Mg-Zn-Zr-Ca alloy with fully recrystallized ultrafine grained structures, *Scr. Mater.*, 2017, 131, 1–5.
- 60 Y. Harai, M. Kai, K. Kaneko, Z. Horita and T. G. Langdon, Microstructural and mechanical characteristics of AZ61 magnesium alloy processed by high-pressure torsion (Reprinted), *Mater. Trans.*, 2008, 49(1), 76–83.
- 61 S. A. Torbati-Sarraf and T. G. Langdon, Properties of a ZK60 magnesium alloy processed by high-pressure torsion, *J. Alloys Compd.*, 2014, **613**, 357–363.
- 62 S. Jayalakshmi, Q. B. Nguyen and M. Gupta, Microstructural and mechanical properties of AZ31 magnesium alloy with Cr addition and CO2 incorporation during processing, *Mater. Chem. Phys.*, 2012, **134**(2–3), 721–727.
- 63 Y. Subasi, Y. Turen, H. Zengin, H. Ahlatci and Y. Sun, Effect of Zn addition on mechanical and corrosion properties of as-cast and as-extruded WE43 magnesium alloys, *Mater. Res. Express*, 2019, 6(11), 14.

- 64 H. Waizy, J. Diekmann, A. Weizbauer, J. Reifenrath, I. Bartsch, V. Neubert, R. Schavan and H. Windhagen, In vivo study of a biodegradable orthopedic screw (MgYREZralloy) in a rabbit model for up to 12 months, *J. Biomater. Appl.*, 2014, 28(5), 667–675.
- 65 H. Windhagen, K. Radtke, A. Weizbauer, J. Diekmann, Y. Noll, U. Kreimeyer, R. Schavan, C. Stukenborg-Colsman and H. Waizy, Biodegradable magnesium-based screw clinically equivalent to titanium screw in hallux valgus surgery: short term results of the first prospective, randomized, controlled clinical pilot study, *Biomed. Eng. Online*, 2013, 12, 62.
- 66 J. H. Gao, S. K. Guan, Z. W. Ren, Y. F. Sun, S. J. Zhu and B. Wang, Homogeneous corrosion of high pressure torsion treated Mg-Zn-Ca alloy in simulated body fluid, *Mater. Lett.*, 2011, **65**(4), 691–693.
- 67 M. Ascencio, M. Pekguleryuz and S. Omanovic, An investigation of the corrosion mechanisms of WE43 Mg alloy in a modified simulated body fluid solution: The effect of electrolyte renewal, *Corros. Sci.*, 2015, 91, 297–310.
- 68 R. Xin, Y. Luo, A. Zuo, J. Gao and Q. Liu, Texture effect on corrosion behavior of AZ31 Mg alloy in simulated physiological environment, *Mater. Lett.*, 2012, 72, 1–4.
- 69 B. Jiang, Q. Xiang, A. Atrens, J. Song and F. Pan, Influence of crystallographic texture and grain size on the corrosion behaviour of as-extruded Mg alloy AZ31 sheets, *Corros. Sci.*, 2017, **126**, 374–380.
- 70 M. Nie, C. T. Wang, M. Qu, N. Gao, J. A. Wharton and T. G. Langdon, The corrosion behaviour of commercial purity titanium processed by high-pressure torsion, *J. Mater. Sci.*, 2014, 49(7), 2824–2831.
- 71 G. Ben Hamu, D. Eliezer and L. Wagner, The relation between severe plastic deformation microstructure and corrosion behavior of AZ31 magnesium alloy, *J. Alloys Compd.*, 2009, 468(1–2), 222–229.
- 72 H. Miyamoto, Corrosion of Ultrafine Grained Materials by Severe Plastic Deformation, an Overview, *Mater. Trans.*, 2016, 57(5), 559–572.
- 73 K. D. Ralston and N. Birbilis, Effect of Grain Size on Corrosion: A Review, *Corrosion*, 2010, **66**(7), 075005.
- 74 N. Saikrishna, G. P. K. Reddy, B. Munirathinam and B. R. Sunil, Influence of bimodal grain size distribution on the corrosion behavior of friction stir processed biodegradable AZ31 magnesium alloy, *J. Magnesium Alloys*, 2016, 4(1), 68–76.
- 75 E. V. Parfenov, O. B. Kulyasova, V. R. Mukaeva, B. Mingo, R. G. Farrakhov, Y. V. Cherneikina, A. Yerokhin, Y. F. Zheng and R. Z. Valiev, Influence of ultra-fine grain structure on corrosion behaviour of biodegradable Mg-1Ca alloy, *Corros. Sci.*, 2020, 163, 108303.
- 76 G. L. Song and A. Atrens, Corrosion mechanisms of magnesium alloys, *Adv. Eng. Mater.*, 1999, 1(1), 11–33.
- 77 Y. Liu, X. Liu, Z. Zhang, N. Farrell, D. Chen and Y. Zheng, Comparative, real-time in situ monitoring of galvanic corrosion in Mg-Mg2Ca and Mg-MgZn2 couples in Hank's solution, *Corros. Sci.*, 2019, **161**, 108185.

78 M. Esmaily, J. E. Svensson, S. Fajardo, N. Birbilis, G. S. Frankel, S. Virtanen, R. Arrabal, S. Thomas and L. G. Johansson, Fundamentals and advances in magnesium alloy corrosion, *Prog. Mater. Sci.*, 2017, 89, 92–193

- 79 J. Liu, Y. Lin, D. Bian, M. Wang, Z. Lin, X. Chu, W. Li, Y. Liu, Z. Shen, Y. Liu, Y. Tong, Z. Xu, Y. Zhang and Y. Zheng, In vitro and in vivo studies of Mg-30Sc alloys with different phase structure for potential usage within bone, *Acta Biomater.*, 2019, 98, 50–66.
- 80 S. Faghihi, F. Azari, A. P. Zhilyaev, J. A. Szpunar, H. Vali and M. Tabrizian, Cellular and molecular interactions between MC3T3-E1 pre-osteoblasts and nanostructured titanium produced by high-pressure torsion, *Biomaterials*, 2007, 28(27), 3887–3895.
- 81 Y. Estrin, H.-E. Kim, R. Lapovok, N. Hoi Pang and J.-H. Jo, Mechanical Strength and Biocompatibility of Ultrafine-Grained Commercial Purity Titanium, *BioMed Res. Int.*, 2013, 914764.
- 82 H. Yilmazer, M. Sen, M. Niinomi, M. Nakai, H. Liu, K. Cho, Y. Todaka, H. Shiku and T. Matsue, Developing biomedical nano-grained beta-type titanium alloys using high pressure torsion for improved cell adherence, *RSC Adv.*, 2016, **6**(9), 7426–7430.

- 83 S. E. Henderson, K. Verdelis, S. Maiti, S. Pal, W. L. Chung, D.-T. Chou, P. N. Kumta and A. J. Almarza, Magnesium alloys as a biomaterial for degradable craniofacial screws, *Acta Biomater.*, 2014, **10**(5), 2323–2332.
- 84 M. M. Gawlik, B. Wiese, V. Desharnais, T. Ebel and R. Willumeit-Roemer, The Effect of Surface Treatments on the Degradation of Biomedical Mg Alloys-A Review Paper, *Materials*, 2018, 11(12), 2561.
- 85 S. Agarwal, J. Curtin, B. Duffy and S. Jaiswal, Biodegradable magnesium alloys for orthopaedic applications: A review on corrosion, biocompatibility and surface modifications, *Mater. Sci. Eng., C*, 2016, **68**, 948–963.
- 86 N. Li and Y. F. Zheng, Novel Magnesium Alloys Developed for Biomedical Application: A Review, *J. Mater. Sci. Technol.*, 2013, **29**(6), 489–502.
- 87 W. Li, Y. Shen, J. Shen, D. Shen, X. Liu, Y. Zheng, K. W. K. Yeung, S. Guan, O. B. Kulyasova and R. Z. Valiev, In vitro and in vivo studies on pure Mg, Mg–1Ca and Mg–2Sr alloys processed by equal channel angular pressing, *Nano Mater. Sci.*, 2020, 2(1), 96–108.
- 88 W. Peng, J. X. Chen, X. F. Shan, Y. C. Wang, F. He, X. J. Wang, L. L. Tan and K. Yang, Mg-based absorbable membrane for guided bone regeneration (GBR): a pilot study, *Rare Met.*, 2019, 38(6), 577–587.